Lightweight composite reflectarray that can be flattened, folded, and coiled for compact stowage

Manan Arya[*], Richard Hodges[†], Jonathan Sauder[‡], Stephen Horst[§], Mehran Mobrem[¶]
Jet Propulsion Laboratory, California Institute of Technology, 4800 Oak Grove Dr, Pasadena, CA 91109

Antonio Pedivellano[‖], Alexander Wen[**], Alan Truong[††] and Sergio Pellegrino[‡‡]
California Institute of Technology, 1200 East California Blvd, Pasadena, CA 91125

Herein is presented a design for a lightweight 5 m × 1 m radio-frequency (RF) reflector that can be flattened, folded, and coiled for compact stowage on board an ESPA-class spacecraft. The reflector is a reflectarray that operates at 3.2 GHz. Compared to state-of-the-art technologies for RF reflectors, the presented design has advantages in terms of areal density, stiffness, deployed stability, and scalability.

Thermal and structural analysis is presented to demonstrate deployed stiffness and thermoelastic stability of the proposed design. Thermal analysis is used to predict in-space deployed temperatures in an operational condition, and structural finite element analysis is used to predict deployed vibration modes and frequencies, and the thermoelastic deformation of the deployed reflector.

Also presented are the fabrication, assembly, and testing of two one-third-scale-length full-scale-width 1.7 m × 1 m test articles. These test articles are used to experimentally demonstrate RF functioning, stowage, deployment, and RF performance after deployment.

I. Introduction

There is a need to develop radio frequency (RF) antenna reflectors for spacecraft that are lightweight, robust, and low-cost. In particular, large-aperture RF reflectors that can stow onboard small spacecraft can enable novel remote-sensing Earth science mission concepts. This paper describes advancements in folded-and-wrapped composite reflectarray technology.

I.A. Implementation Concept

Figure 1 shows the conceptual design of the reflector. To focus the technology development efforts, a point design was chosen: 5 m × 1 m deployed aperture size, operation at a center frequency of 3.2 GHz (S-band), and stowage size compatible with an ESPA-class spacecraft. This size and frequency were chosen to be applicable to a radar mission concept to address the Surface Deformation and Change (SDC) observable specified by the 2018 Earth Science Decadal Survey.[1]

As shown in Figure 1, the reflectarray consists of eight "strips", each 0.12 m wide and 5 m long. Each strip has a cross-section as shown in Figure 1: an ultrathin quartz-epoxy composite structure – consisting of two facesheets separated by a number of "S"-shaped springs – that provides the required separation between the ground plane and the dipole plane of the reflectarray.

---

[*] Technologist, Advanced Deployable Structures. AIAA Senior Member. Manan.Arya@jpl.nasa.gov.

[†] Senior Principal Engineer, Spacecraft Antennas.

[‡] Mechatronics Engineer, Technology Infusion Group, AIAA Senior Member.

[§] RF Microwave Engineer, RF Radar Electronics Group.

[¶] Chief Engineer, Payload and Small Spacecraft Mechanical Engineering Section, AIAA Associate Fellow.

[‖] Graduate Student, Graduate Aerospace Laboratories, MC 105-50. AIAA Student Member.

[**] Graduate Student, Graduate Aerospace Laboratories, MC 105-50. AIAA Student Member.

[††] Research Engineer, Graduate Aerospace Laboratories, MC 105-50.

[‡‡] Joyce and Kent Kresa Professor of Aerospace and Civil Engineering; Jet Propulsion Laboratory Senior Research Scientist; Co-Director, Space-Based Solar Power Project; Graduate Aerospace Laboratories, MC 105-50. AIAA Fellow.

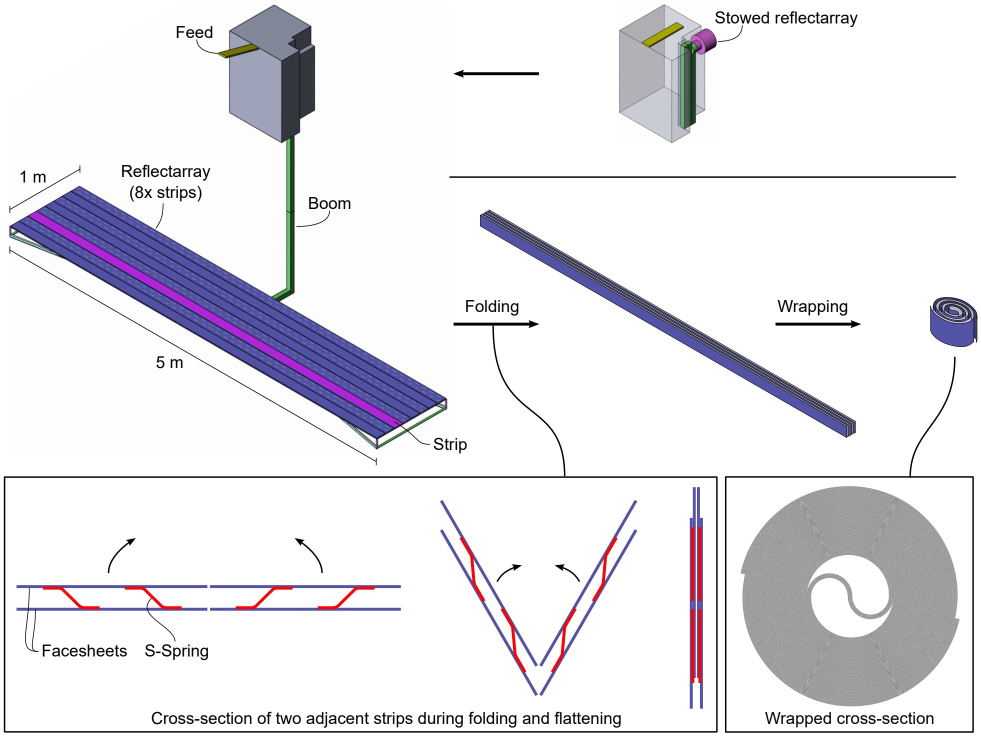

Figure 1: Reflectarray design concept. The reflectarray (in its stowed and deployed configurations) is shown mounted to a conceptual ESPA-class spacecraft bus. The middle row shows the packaging scheme for the reflectarray. The bottom-left inset shows the cross-section of two strips during the first compaction step of folding and flattening, and the bottom-right inset shows a coiled cross-section.

I.B. Packaging Concept

This construction allows the strips to be flattened as they are folded; this is the first step of compaction, illustrated in Figure 1. The strips are folded by means of alternating parallel mountain and valley "slipping folds" (slipping folds allow for relative rotation about and translation along the fold line). Once folded, the "stack" of strips can be coiled; the slipping folds account for relative motion between the strips as they coil around different radii, owing to the non-zero thickness of the flattened strips. This compaction method is called "slip wrapping", and it allows for the elastic, compact, biaxial packaging of bending-stiff structures; this method was described in previous work.[2–4]

I.C. Background

This paper builds on previous work demonstrating a similar reflectarray.[5] The previous reflectarray consisted of strips arranged in concentric squares for a $1.5\,\mathrm{m} \times 1.5\,\mathrm{m}$ aperture, and operated at X-band (8.4 GHz).[5] The current reflectarray has strips arranged parallel to each other, which is more suitable for a long, skinny $5\,\mathrm{m} \times 1\,\mathrm{m}$ aperture, and operates at S-band (3.2 GHz).

Compared to state-of-the-art deployable RF reflectors for small spacecraft, the current approach – based on bending-stiff ultrathin fiber-reinforced composites and slip wrapping – has key advantages.

Compared to solid-panel reflectarrays, where the reflectarray is supported by thick stiff panels hinged to each other (e.g. ISARA[6] and the MarCO high-gain antenna[7]), the current approach has much lower mass. Solid-panel reflectarrays may approach areal densities of $3500\,\mathrm{g\,m^{-2}}$, whereas the current approach could offer a five-fold reduction in mass, with areal densities around $780\,\mathrm{g\,m^{-2}}$. However, this decrease in mass may come at the cost of reduction in thermoelastic stability compared to thick reflectarray panels. Further work on the thermoelastic stability of such structures will mitigate this effect.

Compared to tensioned membrane reflectors,[8,9] the current approach offers higher structural stiffness, thermoelastic stability, and mechanical robustness. These benefits are all due to the use of high-performance low-thermal-expansion fiber-reinforced composite materials that provide stiffness and robustness. Additionally, the current approach has low risk of material creep in a deployed state compared to tensioned polymer membranes. These increases in stiffness and stability come at the cost of increased mass compared to tensioned membranes. Using even thinner composite materials may allow the current concept to approach the lower areal densities of tensioned membrane reflectors.

Finally, compared to mesh-based reflectors (e.g. RainCube's KaPDA reflector[10]), the current approach offers increased robustness, better ground handling properties, and potentially higher scalability. For instance, it would be straightforward to increase the size of the deployed aperture of the current concept by either changing strip dimensions or the number of strips. However, the present approach has lower bandwidth than parabolic mesh-based antennas. Further work is needed, e.g., incorporating dual- or multi-wavelength reflectarray designs with these structural concepts, to increase the bandwidth performance of such reflectors.

I.D. Scope of Paper

This paper focuses on the design, analysis, and testing of the reflectarray surface only. It is recognized that a flight-like implementation of this design would require a deployable support structure for the reflectarray and a deployable boom to provide the separation between the reflectarray and the feed. The design of the support structure and the boom could be based on extensive previous work done on cruciform coilable structures,[11] and on hinged deployable booms.[12] The exact design of this support structure and this deployable boom will be the subject of future work.

This paper is laid out as follows. Section II details the structural design and RF design of the reflectarray. Section III describes numerical and analytical models constructed to capture the thermal and structural behavior of the reflectarray. Section IV describes the fabrication of reflectarray test articles, and the various tests conducted to verify performance. Finally, Section V provides concluding thoughts.

II. Reflectarray Design

This section describes the structural design and the RF design of reflectarray. Both the full-scale $5\,\mathrm{m} \times 1\,\mathrm{m}$ flight concept and the reduced-length $1.7\,\mathrm{m} \times 1\,\mathrm{m}$ test articles are discussed. For this effort, two reduced-length test articles were constructed.

II.A. Structural Design

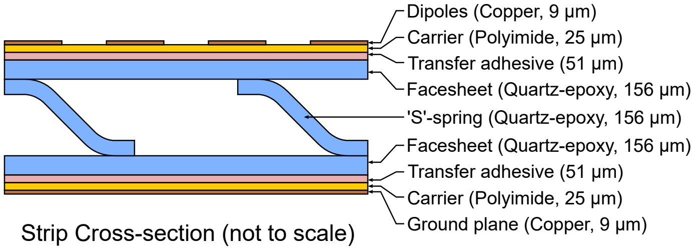

Figure 2: Strip cross section, adapted from previous work.[5]

As shown in Figure 2, each strip has a quartz-epoxy composite structure that provides a stiff, stable, and repeatable reference: there are two facesheets, continuous over the length of the strip, and two rows of S-springs. The S-springs provide 12.7 mm separation between the facesheets, which support the RF ground and dipole planes. The S-springs may be discontinuous over the length of the strip; in fact, current implementation uses 50 mm-long S-springs, spaced at a 90 mm pitch along the length of the strip.

The current facesheet and S-spring construction use a three-ply laminate of ultrathin unidirectional spread-tow plies of amorphous fused quartz fibers (St. Gobain Quartzel) in an epoxy matrix (NTPT TP402). The resin content is 33 %. The cured thickness of the three-ply laminate is about 156 µm. (Three-ply preforms of pre-impregnated spread-tow laminate were purchased from North Thin Ply Technology. Each ply had an areal density of $52\,\mathrm{g\,m^{-2}}$.) For the facesheets, a [90°/0°/90°] laminate is used, and for the S-springs, a [0°/90°/0°] laminate is used; 0° being along the length of the strip. This laminate design was thought to reduce the fiber strain in the facesheets during coiling (since the 0° ply is not at the surface of the facesheet), and to reduce the fiber strains in the S-springs during flattening (since the 90° ply is not at the surface of the S-spring). Alternative laminate design (possibly with a higher number of plies) may be used. (Of course, to maintain low mass density, for a higher number of plies, thinner and lighter spread-tow plies of unidirectional quartz-epoxy must be used.)

The strips are connected to each other using "ligaments" that implement the slipping folds. These ligaments are small lengths of cord that provide some connection between the strips while allowing for the rotation and translation degrees of freedom for the slipping folds. At either end of the 5 m length of the array, the strips are connected to each other using elements called "tension parabolas". These tension parabolas take four corner forces applied by the separate support structure and redistribute these corner forces to lengthwise tension along each strip. The notional design of the support structure is illustrated in Figure 3; it consists of four coilable composite booms, and two secondary struts. This structure is deployable, and its exact design will be the subject of future work.

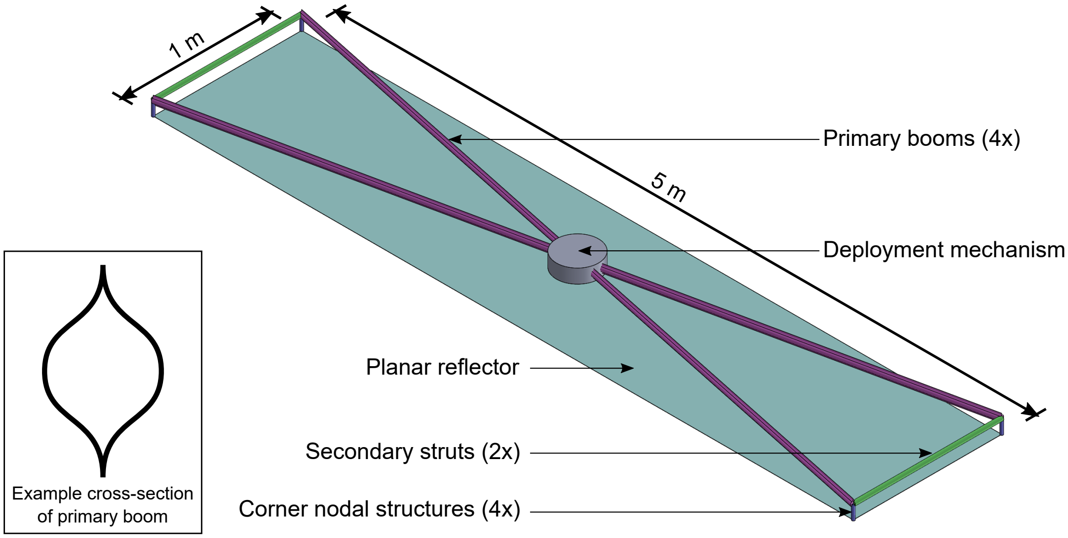

Figure 3: Reflectarray support structure.

II.B. RF Design

The reflectarray was designed to have a center frequency of 3.2 GHz and a designed bandwidth of 50 MHz. The reflectarray consists of a plane of dipoles parallel to a ground plane; these two planes are separated 13.2 mm apart. The dipoles are arranged in a rectangular grid, with equal 59 mm spacing along the two orthogonal in-plane axes. For the full-scale 5 m × 1 m flight concept, there are 84 × 16 dipoles; for the reduced-scale 1.7 m × 1 m test articles, there are 28 × 16 dipoles. The size of each dipole is adjusted according to its position in the aperture to provide the appropriate phase delay for beam collimation.

The reflectarray was designed to have a 3.5 m focal length. Test Article 1 was designed to be center fed, whereas Test Article 2 was designed to be offset fed, with the feed situated 30° off-normal in the elevation plane. Section IV describes the RF test configurations used for the two test articles in further detail.

III. Modeling and Analysis

III.A. Thermal Models

For both thermal models – the simple analytical model and the more complex finite element model – the primary intent was to estimate the temperature differential between the sun-side facesheet and the anti-sun-side facesheet; this temperature differential is the key parameter needed for predicting, to first order, the thermoelastic deformation of the deployed reflectarray.

The assumed orbit is an 800 km dawn-dusk sun-synchronous orbit; this places the spacecraft directly above the terminator at all times. The orientation of the reflector is assumed as follows: the long axis of the reflector is aligned with the satellite velocity vector, and the reflector is pointed off-nadir by some side-look angle between ±35°. For this choice of orbit and orientation, the side-look angle and the solar incidence angle (the angle between the reflector normal and the sun vector) sum to 90°, i.e., for zero side-look angle, the sun is edge-on to the reflector. In an operational setting, the worst-case temperature differential between the two facesheets is expected to occur at the minimum solar incidence angle of 55°, i.e., when the sun is most normal to the reflector. For additional 10° margin, the thermal models assume a solar incidence angle of 45°.

III.A.1. Simplified Two-Node Thermal Model

An analytical thermal model of the deployed reflectarray was constructed. For simplicity, this model assumes homogeneous material properties, temperatures, and loading conditions. Each facesheet is modeled as a single node, with various incoming and outgoing thermal fluxes, as shown in Figure 4. Further simplifying assumptions include neglecting the effects of Earth albedo and Earth infrared emissions, and that the temperature of deep space is 0 K.

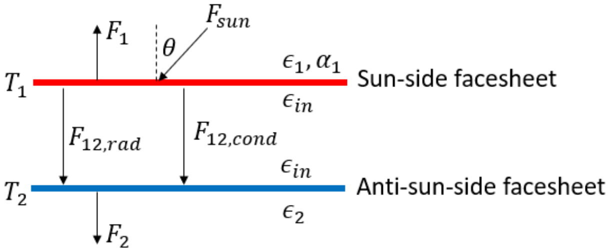

Figure 4: Simplified Thermal Model.

This model accounts for the incident solar flux $F_{sun} = \alpha_1 G_s \cos\theta$ (where α_1 is the solar absorption coefficient of the sun-facing surface, $G_s = 1370\,\mathrm{W\,m^{-2}}$ is the solar constant, and θ is the solar incidence angle), the radiation to deep space of the two outward facing surfaces $F_1 = \epsilon_1 \sigma T_1^4$ and $F_2 = \epsilon_2 \sigma T_2^4$ (where ϵ is the emissivity of the surface, $\sigma = 5.67 \times 10^{-8}\,\mathrm{Wm^{-2}K^{-4}}$ is the Stefan-Boltzmann constant, and T is the homogeneous facesheet temperature), the radiative flux between the two facesheets $F_{12,rad} = \frac{\epsilon_{in}}{2-\epsilon_{in}}\left(T_1^4 - T_2^4\right)$ (where ϵ_{in} is the emissivity of the two inward facing faces), and the conductive flux between the two facesheets through the S-springs $F_{12,cond} = \frac{k}{h}\left(T_1 - T_2\right)$ (where k is the area-homogenized S-spring conductivity and h is the separation between the two facesheets).

By writing Krichhoff's laws for the two facesheets, one obtains a system of two equations and two unknown steady-state temperatures that can be solved numerically. In the case of negligible thermal conduction between the two facesheets, there is an analytical solution. For this particular structure, the thermal conduction through the S-springs appears to be negligible: the fractional in-plane area of the S-springs available for thermal conduction between facesheets is 1.37×10^{-3}, and the estimated thermal conductivity of the quartz-epoxy material (using an upper bound that is the thermal conductivity of pure fused quartz) is $1.32\,\mathrm{W\,m^{-1}\,K^{-1}}$, leading to $k = 1.81 \times 10^{-3}\,\mathrm{W\,m^{-1}\,K^{-1}}$, which is small enough to be neglected.

Parameter	**Symbol**	**Material**	**Value**
Sun-facing absorption coefficient	α_1	10% copper + 90% polyimide	0.395
Sun-facing emissivity	ϵ_1	10% copper + 90% polyimide	0.814
Interior emissivity	ϵ_{in}	Bare quartz-epoxy	0.93
Anti-sun-facing emissivity	ϵ_2	Matte copper	0.04

Table 1: Thermo-optical parameters of the surfaces assuming polyimide properties $\alpha = 0.41$ and $\epsilon = 0.9$.

The values in Table 1 are used for the various thermo-optical parameters in this model. For these parameters, for a solar incidence angle of 45°, a temperature differential of 3.3 K was obtained between the top and bottom facesheets.

This simplified thermal model, though not entirely accurate in predicting absolute temperatures or temperature differentials (compared to the thermal finite element model discussed below), is a useful tool in performing preliminary design of such structures and assessing the sensitivity to various parameters.

III.A.2. Thermal Finite Element Model

A high-fidelity finite element thermal model of the deployed reflector in its nominal configuration was created in Thermal Desktop. As shown in Figure 5, this model includes the geometry of the facesheets and the separate S-springs. Given this separate modeling of individual S-springs, the homogenization approach to modeling thermal conduction through S-springs discussed in Section III.A.1 is not needed. In addition to relaxing this homogenization assumption, the high-fidelity thermal model includes the effects of Earth albedo and Earth infrared emission, and of the finite temperature of deep space. Further, this model makes no assumptions about the homogeneity of the facesheet temperature, or of the homogeneity of the loading conditions.

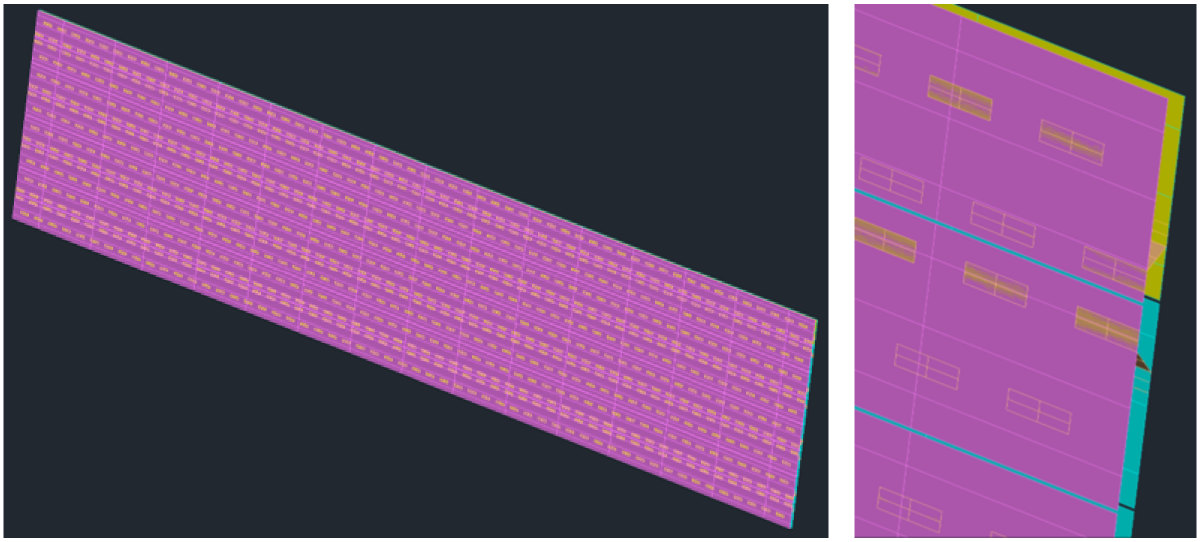
(a) (b)

Figure 5: Thermal Desktop model.

This high-fidelity thermal model was used to conduct parameter sweeps of various values, and assess the effects of e.g., Earth albedo, edge effects, and the localized thermal conduction effects of the S-springs. For the thermo-optical properties indicated in Table 1 and for a solar incidence angle of 45°, this model predicts that the difference between the spatially averaged temperatures of the two facesheets is 10 K. This is reasonable compared to the prediction of 3.3 K of the simple model described in Section III.A.1, considering that the addition of Earth albedo and Earth infrared emissions will add incoming thermal flux.

Additionally, it can be noted from the predictions of this model that the assumption of temperature homogeneity in Section III.A.1 is adequate for these initial analyses; as shown in Figure 6, the facesheet temperatures are uniform to within approximately 15 K. For the thermoelastic deformation that follows in Section III.B, the facesheet temperature is assumed to be homogeneous, with a uniform temperature differential of 10 K (as predicted by the high-fidelity model) between the two facesheets. For future analyses, however, the edge effects and the localized effects of S-springs ought to be considered in predicting thermoelastic deformations.

III.B. Structural Finite Element Model

A structural finite element (FE) model of the deployed reflector was constructed in Abaqus/Standard 2018. This model was used to study the deployed natural (structural) frequencies of the reflector, and the thermoelastic deformations of the reflector.

The facesheets and S-springs were modeled using S4R reduced-integration shell elements. Homogeneous isotropic material properties were used; these were calculated based on classical lamination theory (CLT) and the laminate design. In general, CLT predicts two different in-plane laminate material properties; for the FE model, the worst-case CLT predictions were used i.e., the lowest in-plane modulus and the highest in-plane coefficient of thermal expansion (CTE). Table 2 lists the various material properties used for the FE model.

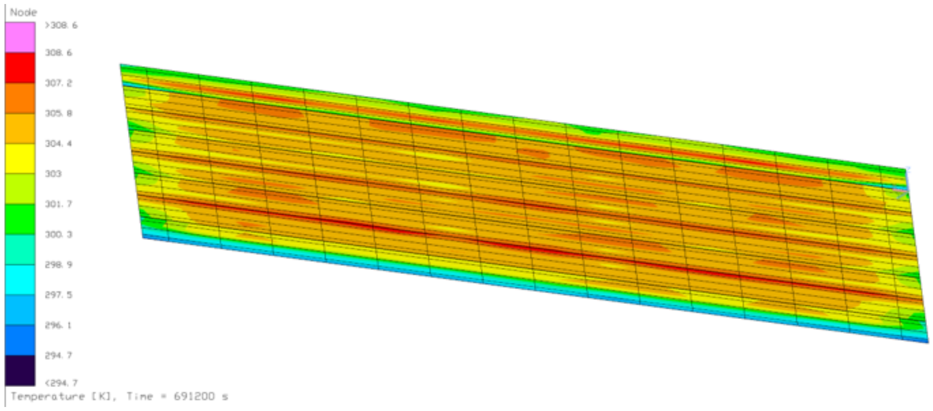

(a) Sun-side facesheet

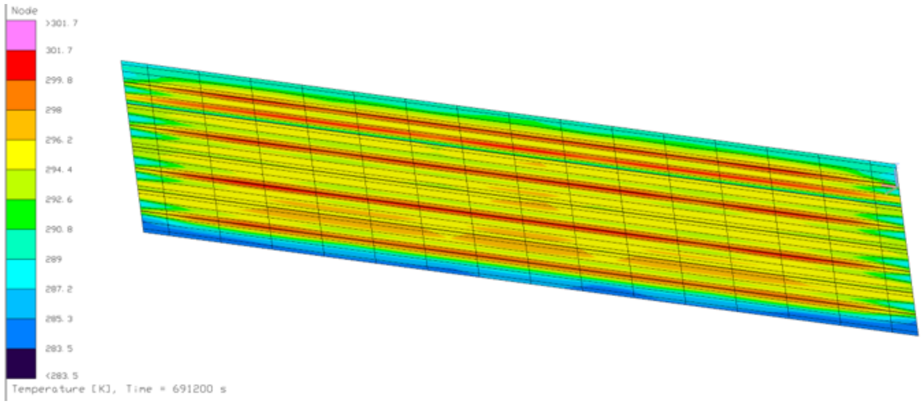

(b) Anti-sun-side facesheet

Figure 6: Thermal Desktop model results for a sun angle of 45°.

Parameter	**Value**	**Source**
Laminate modulus	22.9 GPa	Minimum in-plane CLT prediction
Laminate Poisson's ratio	0.054	CLT prediction
Laminate CTE	$5.44 \times 10^{-6}\,\mathrm{K}^{-1}$	Maximum in-plane CLT prediction
Facesheet density	$1.795\,\mathrm{kgm}^{-3}$	Accounts for mass of laminate & RF planes
S-spring density	$1.000\,\mathrm{kgm}^{-3}$	Accounts for mass of laminate
Lamina 0° modulus	49.4 GPa	Rule of mixtures
Lamina 90° modulus	9.5 GPa	Rule of mixtures
Lamina 0° CTE	$1.33 \times 10^{-6}\,\mathrm{K}^{-1}$	Rule of mixtures
Lamina 90° CTE	$15.16 \times 10^{-6}\,\mathrm{K}^{-1}$	Rule of mixtures
Resin content	33%	Vendor provided
Cured ply thickness	52 µm	Measured 3-ply cured thickness: 156 µm
Fiber modulus	72 GPa	Saint Gobain Quartzel datasheet[13]
Fiber CTE	$0.54 \times 10^{-6}\,\mathrm{K}^{-1}$	Saint Gobain Quartzel datasheet[13]
Matrix modulus	3.44 GPa	NTPT TP402 datasheet[14]
Matrix CTE	$35 \times 10^{-6}\,\mathrm{K}^{-1}$	Based on other epoxy matrices

Table 2: Material properties used for the structural FE model

The facesheets and the S-springs were modeled as separate parts. The S-spring surfaces were tied to the appropriate facesheet surfaces using surface-to-surface tie constraints. The tension parabolas were modeled using T3D2 truss elements, and were tied to the facesheets using pinned multi-point constraints. The ligaments between the strips are not modeled here; this leads to further conservatism in the analysis, as these ligaments are expected to stiffen the structure.

The elements, once initialized, have no pre-stress. As such, the structure is quite compliant at the outset. To stabilize the structure during the pre-tensioning process, low-rate springs connect all nodes in the tension parabolas to ground at the outset. These low-rate springs are implemented using connector elements. In the first step of analysis, a set of loads and boundary conditions (shown in Figure 7) is applied to the structure to introduce pre-tension in the tension parabolas and strips. In the second step of analysis, the stiffness of the stabilizing low-rate springs is slowly degraded to zero (using an Abaqus model change procedure) to produce a equilibrium tensioned configuration. After this, the third step is either a frequency step to extract the natural structural frequencies, or a static step to determine the thermoelastic deformation due to an applied through-thickness temperature gradient. The non-linear geometry option (NLGEOM) is used throughout.

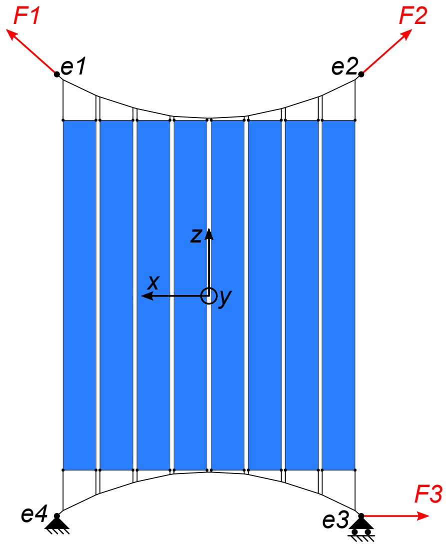

Figure 7: Forces and boundary conditions applied to pre-tension the reflectarray. Note that the four end points of the tension parabolas e_1 through e_4 are further constrained to be in the x, z plane.

The results presented here are for an applied tension of 11.6 N in each strip. Figure 8 shows the predicted second mode shape for the deployed reflectarray, which has a natural frequency of 1.69 Hz. The first mode of the deployed reflectarray has a frequency of 1.02 Hz; however, this mode is localized to the tension parabolas and their connection to the strips, and ought to be removed or raised in frequency through further design iteration. The second mode is the lowest mode dominated by out-of-plane bending of the strips, which will influence reflector performance much more than localized edge modes.

Figure 9 shows the predicted out-of-plane thermoelastic deflection of the reflectarray due to an imposed through-thickness temperature gradient of 10 K. This is the worst-case predicted temperature gradient during operations. As expected (for a bending-stiff structure with a through-thickness gradient), the deflected reflectarray adopts a bowed shape under this thermoelastic deformation. The maximum out-of-plane deflection is 12.2 mm, which is 0.13 times the RF wavelength. Further design changes (e.g., changing the laminate to have more longitudinal fibers) may be required to reduce this deflection. For instance, the predicted maximum out-of-plane deflection reduces to 5.7 mm assuming a [0°/90°/0°] laminate for the facesheets, as opposed to the current [90°/0°/90°] laminate.

Note that the structural FE results shown here do not include the reflectarray support structure as described in Section II.A. Further work is required to design and implement this support structure in these FE models. The support structure, while much stiffer than the reflectarray, will regardless lead to a decrease in stiffness over the ideal boundary conditions applied here.

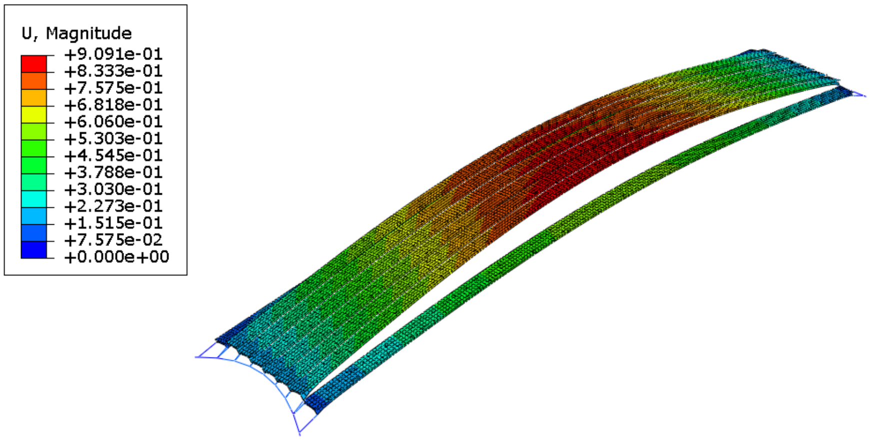

Figure 8: Predicted second mode shape for the reflectarray at 1.69 Hz.

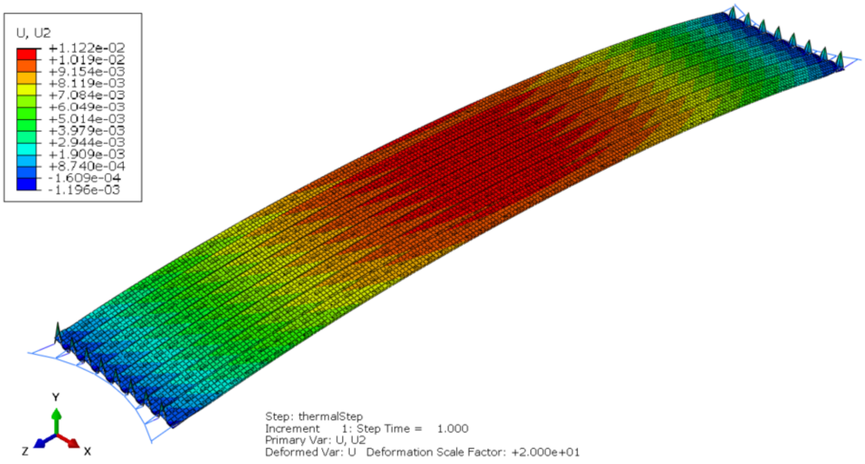

Figure 9: Predicted out-of-plane deflections for an imposed through-thickness 10 K temperature gradient. This is the worst-case operational temperature gradient, as predicted in Section III.A. The deflection is plotted in units of meters.

IV. Testing and Results

Two one-third-length full-width 1.66 m × 0.94 m reflectarray test articles were constructed and tested. Table 3 lists the dates for the fabrication, assembly, and testing of these two test articles. Test Article 1 was constructed and RF-tested. Due to a manufacturing defect, Test Article 1 could not be stowed and deployed; as such, it was used only for validating the RF performance. Test Article 2 corrected the manufacturing defect, and was RF tested before and after a test of stowage and deployment. The subsections below describe the fabrication and testing of the two test articles.

Dates	**Test Article**	**Activity**
2020-08-25 to 2020-09-20	Test Article 1	Fabrication and assembly
2020-09-21 to 2020-09-23	Test Article 1	RF testing
2020-12-15 to 2021-08-21	Test Article 2	Fabrication and assembly
2021-09-08	Test Article 2	Pre-stowage RF test
2021-09-13	Test Article 2	Stowage and deployment test
2021-09-13 to 2021-09-15	Test Article 2	Post-stowage RF testing

Table 3: Testing timeline

IV.A. Test Article Fabrication and Assembly

The two reflectarray test articles represent the center one-third of the full-scale reflectarray design, and measure 1.66 m in length and 0.94 m in width. The reduced length was chosen to expedite schedule and reduce cost.

Broadly speaking, there are two steps to producing reflectarray test articles: first, fabrication of 1.67 m-length quartz-epoxy strips, and second, assembling eight strips by attaching the dipole plane, the ground plane, and the tension parabolas.

The quartz-epoxy strips were fabricated using three-ply [90°/0°/90°] preforms of spread-tow unidirectional plies of Quartzel fibers preimpregnated with a TP402 epoxy matrix. These preforms were procured from North Thin Ply Technologies (NTPT). As shown in Figure 10, compliant silicone molds encased in a stiff aluminum tool were used to support the preforms during the single high-temperature cure. Consolidation pressure is applied by the differential CTE of the silicone molds against the aluminum tool; as such, autoclave pressure is not needed. This fabrication method has been described in previous work.[5,15]

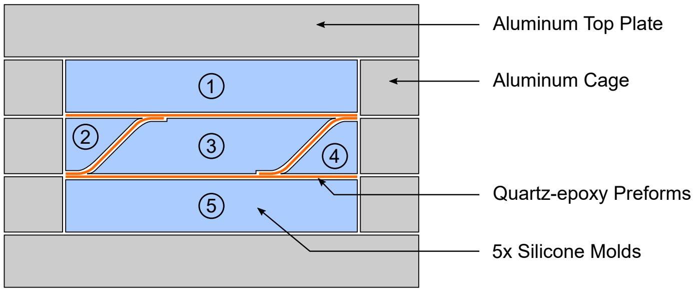

Figure 10: Cross-section of a single strip during fabrication, adapted from previous work.[5]

The dipole plane was made by photochemical etching of DuPont Pyralux film (part number AC092500E), which consists of a 9 µm-thick layer of copper on a support layer of 25 µm-thick polyimide film. The ground plane was realized as unetched Pyralux film. The dipole plane and the ground plane were attached to the facesheets of the cured quartz-epoxy composite strips using 51 µm-thick acrylic transfer adhesive (3M F9460PC). The tension parabolas were laser-cut 51 µm-thick polyester sheets; the tension parabolas were attached to the strips using Kapton tape. The ligament connections between the strips were implemented using glass-fiber-reinforced packing tape; for each pair of adjacent strips, two ligaments along the length of the interface were implemented: each ligament 0.42 m from an end of the strips.

The mass of each reflectarray test article was measured, and is reported in Table 4, along with the calculated areal densities.

Test Article	**Mass** (g)	**Areal density** ($\mathrm{g\,m^{-2}}$)
Test Article 1	1207	772
Test Article 2	1234	787

Table 4: Test article measured masses and calculated areal densities

For the test articles, a non-deployable bow-tie-shaped support structure was assembled using off-the-shelf glass-fiber-reinforced-polymer (GFRP) tubes and 3D-printed plastic nodes (see Figure 13). Constant-force springs were used to apply equal tensions to the four ends of the tension parabolas. For Test Article 1, a nominal tension of 10 N was applied at each corner, leading to a nominal tension of 1.1 N in each strip. For Test Article 2, a nominal tension of 17.5 N was applied at each corner, leading to a nominal tension of 1.9 N in each strip.

IV.A.1. Single-Strip Coiling Tests

To qualify fabricated strips before assembly, individual strips were coiled and uncoiled using a single-strip coiling mechanism. This process verified the ability of a strip to sustain coiling strains without damage. As shown in Figure 11, this coiling mechanism consists of a central drum (100 mm diameter) on which the strip is coiled, a co-coiled overwrap membrane that is tensioned and provides radially inwards pressure on the strip, and a membrane tensioning system. The membrane tensioning system consists of a membrane roller that unspools the membrane during coiling; this roller is driven by a motor driven in a constant-torque feedback loop, which maintains constant tension on the membrane. The central drum is rotated by a second motor in an open-loop fashion. This mechanism follows closely the design of similar stowing mechanisms for bending-stiff coilable shell structures described previously.[16]

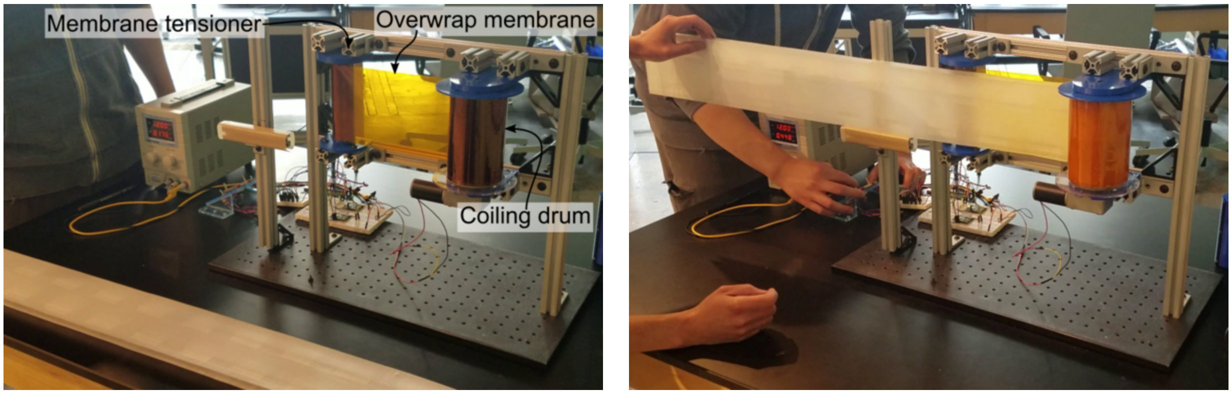

(a) (b)

Figure 11: Single-strip coiling mechanism.

IV.B. RF Testing

RF testing of both test articles was conducted at the JPL Mesa Antenna Test Facility, using a planar near-field scanner. Figure 12 shows the configuration of these RF tests. The test article was illuminated at a 30° angle to accommodate the 3.5 m focal length within the available space. Test Article 1 was designed to be center-fed, and so this configuration resulted in a loss of performance. Test Article 2, though, was designed to be illuminated at a 30° degree scan angle, exactly as in the test configuration.

Figure 13 shows Test Article 1 mounted in the anechoic chamber of the near-field range. The prototype support structure was held by its central node using a metallic fixture; this allowed the bottom edge of the reflectarray to be approximately 1 m above the floor. Given the orientation of the test article in this test, with gravity aligned with the strip lengths, no additional gravity offload was required to stabilize the structure of the reflectarray.

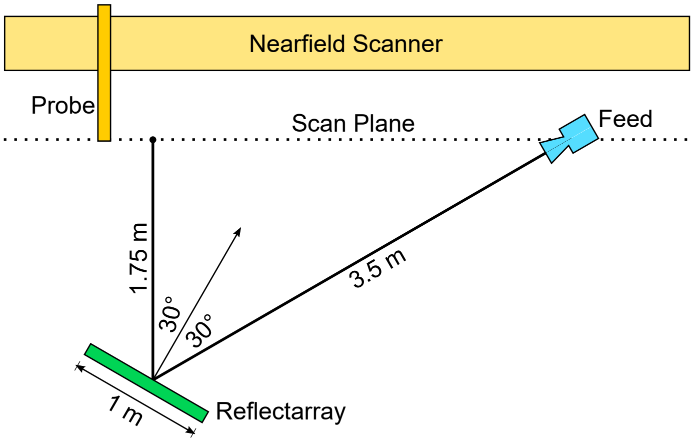

Figure 12: RF test configuration.

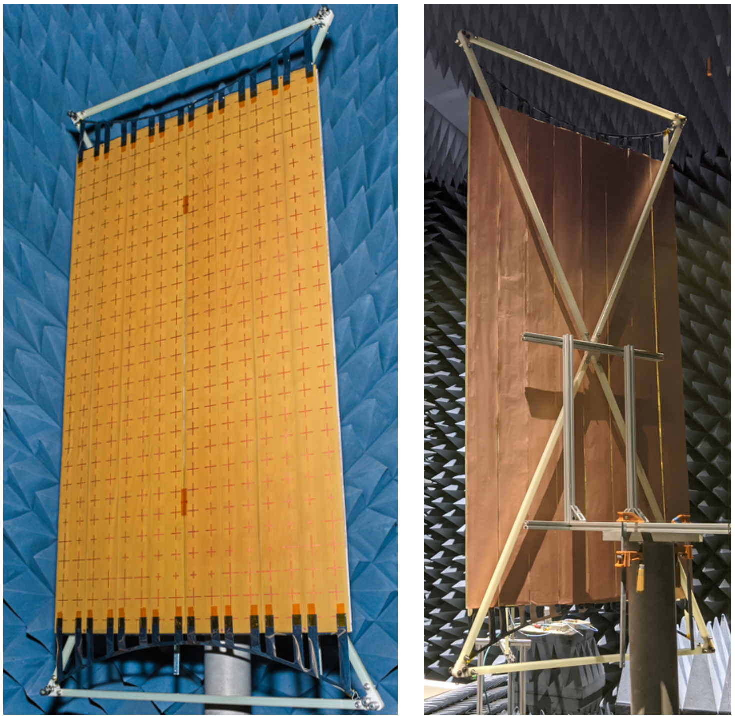

(a) Front view

(b) Rear view

Figure 13: RF test of Test Article 1.

For the Test Article 1 RF test, a MI-212-2.6 standard gain horn was used as a feed; this resulted in a sub-optimal illumination pattern and thus high side-lobe levels. Figure 14 shows azimuth and elevation cuts through the measured far-field antenna patterns, as well as predicted antenna patterns. Despite the sub-optimal feed and scan angle, the measured results match the predictions well.

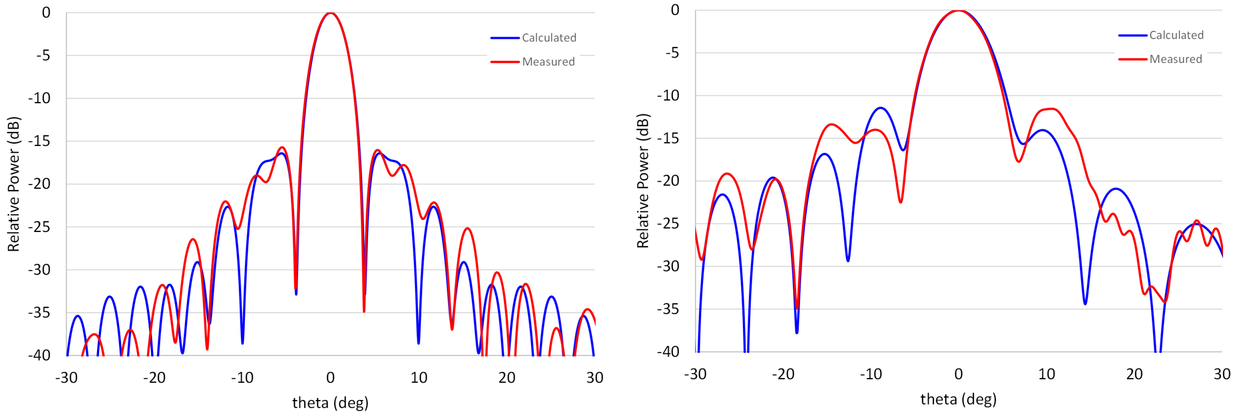

(a) Azimuth (b) Elevation

Figure 14: RF test results and model predictions for Test Article 1.

RF testing for Test Article 2 incorporated lessons learned from RF testing for Test Article 1. This included designing the reflectarray to be offset-fed (as in the RF test configuration, see Figure 12), and incorporating a custom-designed patch array to be used as feed for illuminating the reflectarray. Additionally, RF testing of Test Article 2 was conducted before and after stowage to quantify the effects of such stowage on RF performance. (This could be done because Test Article 2 rectified the manufacturing errors that lead to Test Article 1 being unable to stow.) As shown in Figure 15, there is less than $-20\,\mathrm{dB}$ of difference between the two antenna patterns, indicating that the reflectarray RF performance does not degrade due to stowage and deployment. Indeed, this level of difference in the antenna patterns was also seen between successive RF tests where the reflectarray test article was simply removed from the support structure and re-mounted in the RF test chamber, without stowing the reflectarray. As such, this small difference could be due entirely to repeatability errors in re-mounting the reflectarray.

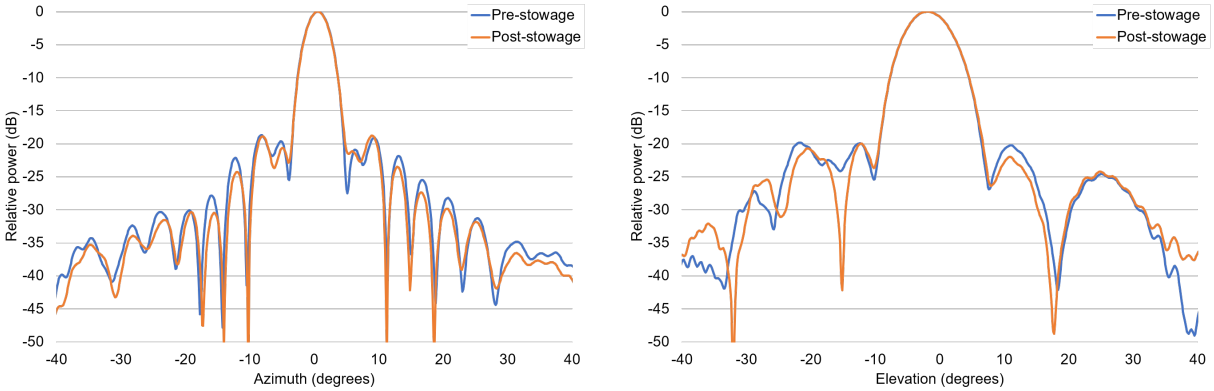

(a) (b)

Figure 15: RF test results for Test Article 2, before and after stowage.

IV.C. Stowage and Deployment Testing

After the pre-stow RF test, Test Article 2 was transported to Caltech for stowage and deployment testing. As shown in Figure 1, there are two stowage steps: first, folding (during which the reflectarray flattens), and second, coiling. For deployment, these steps are reversed. Test Article 2 was folded manually, and a narrow tape was looped around center of the folded stack of strips to keep the reflectarray folded. After folding, Test Article 2 was coiled using a mechanism.

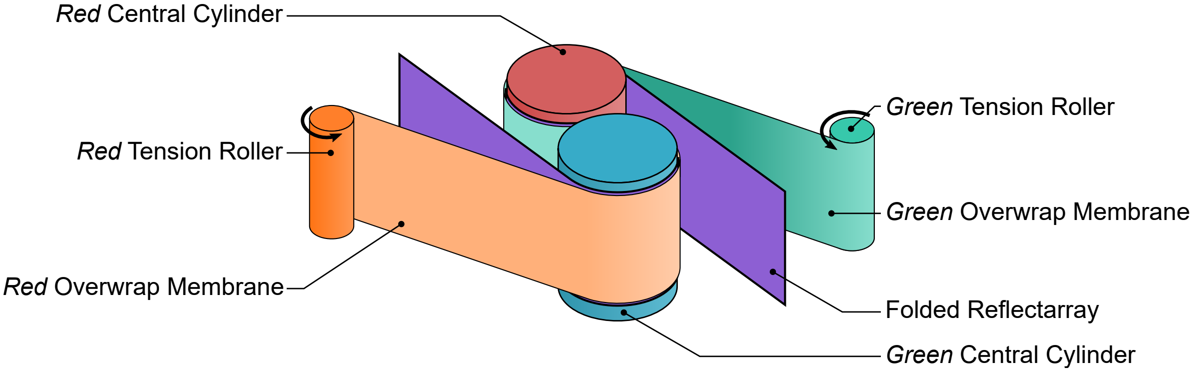

Figure 16: Reflectarray coiling mechanism.

The design of this mechanism is illustrated in Figure 16. This mechanism uses two overwrap tension membranes (denoted *red* and *green* in Figure 16) to apply radially inwards pressure on the folded stack of bending-stiff strips to consolidate and coil them in an 'S' shape. Two central cylinders (of 100 mm diameter each) react the radially inwards pressure of the tension membranes and constrain the coiling radius of the reflectarray strips. Each overwrap tension membrane terminates at the corresponding central cylinder (appropriately coded *red* and *green* in Figure 16). Each overwrap membrane tensioned by a tension roller; this roller has a pre-determined torque applied to it by a motor. The two central cylinders are attached to a platter at the bottom. A stepper motor rotates this platter to coil and uncoil the structure. The design of this mechanism and the approach of using tensioned membranes to coil and consolidate shell structures follows previous work.[16]

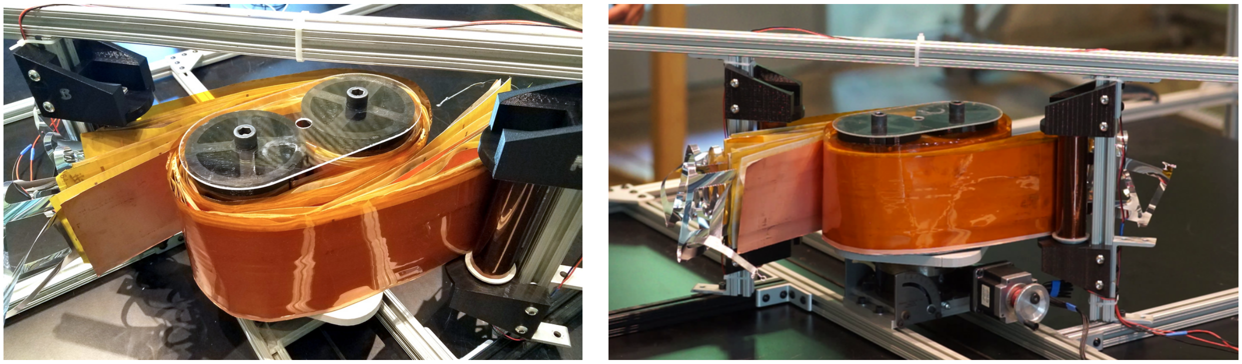

(a) (b)

Figure 17: Stowed reflectarray Test Article 2.

Figure 17 shows the stowed reflectarray Test Article 2. The coiled reflectarray had approximate dimensions 250 mm width, 200 mm depth, 125 mm height. Note that this does not represent a very well-compacted state; further compaction could be achieved by increasing the tension in the overwrap membrane, and by increasing the degree of rotation of the central platter. These steps of further compaction were not taken, since this was the first time Test Article 2 was fully coiled, and it was desired to minimize the risk of damage to the structure. Future testing will attempt to coil such structure more compactly.

After stowage, Test Article 2 was deployed using the same mechanism, as shown in Figure 18. There are two steps of deployment: first, uncoiling, and second, unfolding. The four ends of the tension parabolas on the reflectarray were attached to cord retractors attached to the corners of a rectangular frame (representing a deployed support structure), and the platter was driven in the reverse direction. The overwrap membranes remained tensioned throughout deployment. At the end of uncoiling, the reflectarray was in a "bow-tie" shape, held folded and flattened at the center by the two central cylinders and the loop of tape previously

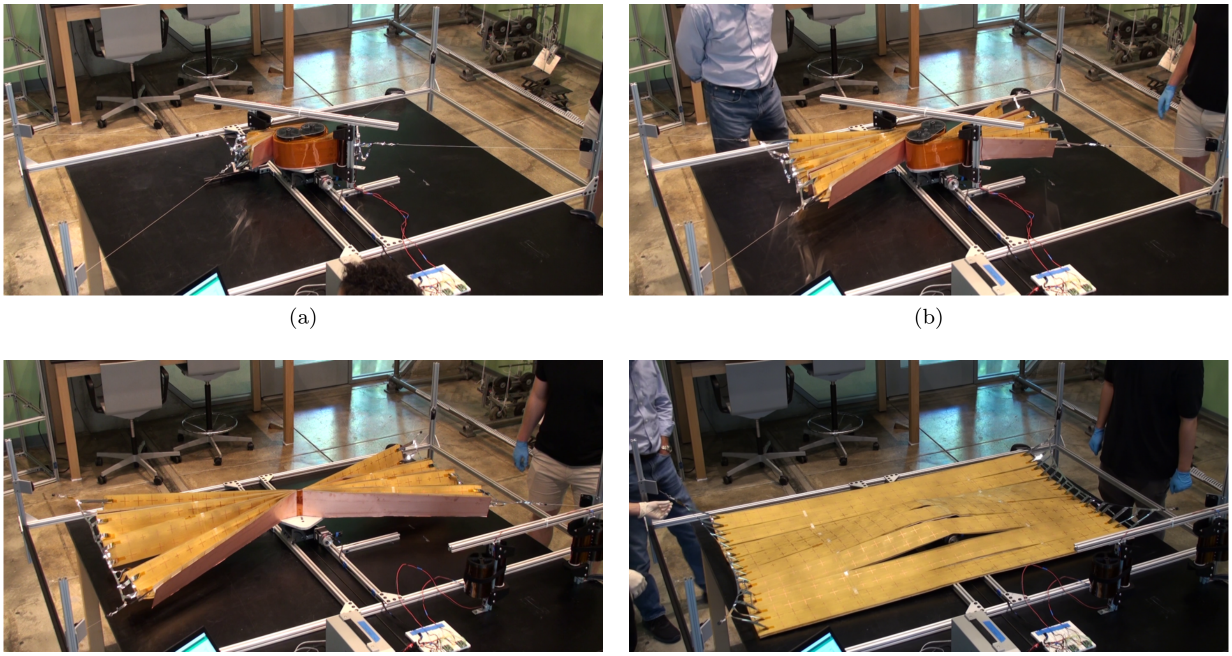

(a) (b) (c) (d)

Figure 18: Deployment of Test Article 2.

installed. The central cylinders, the overwrap membranes, and the tension rollers were then manually removed. (For a flight-like design, this removal of the cylinders, the membranes, and the rollers would be mechanized.) After this, the loop of tape was cut, allowing the reflectarray to unfold. Since no gravity offload was used, the unfolded reflectarray was drapped over the table and the central platter.

After deployment, Test Article 2 was taken back to JPL and re-mounted at the Mesa Antenna Test Range, and its RF performance was measured, as discussed in Section IV.B. No significant degradation of RF performance was noted due to this stowage-and-deployment process.

V. Conclusions

This paper presented a design architecture for a lightweight $5\,\mathrm{m} \times 1\,\mathrm{m}$ reflectarray at 3.2 GHz that can be flattened, folded, and coiled for compact stowage. The feasibility of this design was demonstrated through analysis and testing.

Preliminary thermal and structural analysis was conducted to demonstrate the deployed stiffness and thermoelastic stability of the reflectarray. Two one-third-scale-length full-scale-width $1.7\,\mathrm{m} \times 1\,\mathrm{m}$ test articles were fabricated; RF functioning (before and after stowage), stowage, and deployment were demonstrated experimentally using these test articles.

To further mature this design, additional analysis and testing is needed. Design and analysis of a deployable support structure – which is within demonstrated capabilities – ought to be conducted. Subsystem-level analysis (i.e., of the deployed reflectarray with the support structure) must be conducted. Maturation of the design of the deployment mechanism – which was demonstrated at the prototype level here – will also be needed. Finally, full-scale reflectarray prototypes ought to be constructed and tested.

Acknowledgments

JPL intern Nicholas Saltarelli designed the aluminum tooling needed to fabricate the stripes. Ray Quintero at JPL drafted the reflectarray patterns. Jefferson Harrell at the JPL Mesa Antenna Test Range helped set up and run the RF tests. Kevin Anderson at JPL helped set up and run the Thermal Desktop model. Many thanks to John Pederson and Brayden Aller at Caltech for help with the stowage and deployment tests.

Many thanks to all involved who supported this work during the challenging COVID-19 pandemic.

A part of this research was carried out at the Jet Propulsion Laboratory, California Institute of Technology, under a contract with the National Aeronautics and Space Administration (80NM0018D0004).

References

[1] National Academies of Sciences, Engineering, and Medicine, *Thriving on Our Changing Planet: A Decadal Strategy for Earth Observation from Space*, The National Academies Press, Washington, DC, 2018.

[2] Arya, M., *Packaging and Deployment of Large Planar Spacecraft Structures*, Ph.D. thesis, California Institute of Technology, 2016.

[3] Arya, M., Lee, N., and Pellegrino, S., "Ultralight structures for space solar power satellites," *3rd AIAA Spacecraft Structures Conference*, 2016.

[4] Arya, M., Lee, N., and Pellegrino, S., "Crease-free biaxial packaging of thick membranes with slipping folds," *International Journal of Solids and Structures*, Vol. 108, 2017, pp. 24–39.

[5] Arya, M., Sauder, J., Hodges, R., and Pellegrino, S., "Large-area deployable reflectarray antenna for CubeSats," *6th AIAA Spacecraft Structures Conference*, 2019.

[6] Hodges, R. E., Chahat, N. E., Hoppe, D. J., and Vacchione, J. D., "A Deployable High-Gain Antenna Bound for Mars: Developing a new folded-panel reflectarray for the first CubeSat mission to Mars," *IEEE Antennas and Propagation Magazine*, Vol. 59, No. 2, 2017, pp. 39–49.

[7] Chahat, N. E., Agnes, G., Sauder, J. F., and Cwik, T., "One Meter Deployable Reflectarray Antenna for Earth Science Radars," *2017 IEEE Antennas and Propagation Society International Symposium Proceedings*, 2017.

[8] Warren, P. A., Steinbeck, J. W., Minelli, R. J., and Mueller, C., "Large, Deployable S-Band Antenna for a 6U Cubesat," *29th Annual AIAA/USU Conference on Small Satellites*, 2015.

[9] Kelly, P. K., "A Scalable Deployable High Gain Antenna - DaHGR," *AIAA/USU Conference on Small Satellites*, 2016.

[10] Chahat, N. E., Hodges, R. E., Sauder, J., Thomson, M., Peral, E., and Rahmat-Samii, Y., "CubeSat Deployable Ka-Band Mesh Reflector Antenna Development for Earth Science Missions," *IEEE Transactions on Antennas and Propagation*, Vol. 64, No. 6, 2016, pp. 2083–2093.

[11] Wilkie, W. K., Fernandez, J. M., Stohlman, O. R., Schneider, N. R., Dean, G. D., Kang, J. H., Warren, J. E., Cook, S., Brown, P. L., and Denkins, T. C., "Overview of the NASA Advanced Composite Solar Sail System (ACS3) Technology Demonstration Project," *AIAA Scitech 2021 Forum*, Jan. 2021.

[12] Lytal, P. and Renson, M., "Spacecraft Common Deployable Boom Hinge Deploy and Latching Mechanisms," *Proceedings of the 44th Aerospace Mechanisms Symposium*, May 2018.

[13] Saint-Gobain Quartz SS, "Saint Gobain Quartzel datasheet," 2020.

[14] North Thin Ply Technologies, "NTPT ThinPreg 402 datasheet v1.6," 2017.

[15] Schlothauer, A., Royer, F., Pellegrino, S., and Ermanni, P., "Flexible Silicone Molds for the Rapid Manufacturing of ultra-thin Fiber Reinforced Structures," *Society for the Advancement of Material and Process Engineering (SAMPE 2018)*, 2018.

[16] Gdoutos, E. E., Truong, A., Pedivellano, A., Royer, F., and Pellegrino, S., "Ultralight Deployable Space Structure Prototype," *7th AIAA Spacecraft Structures Conference*, 2020.